



**AALBORG UNIVERSITY**  
DENMARK

**Aalborg Universitet**

## **A Systematic Control Design Method with Active Damping Control in Voltage Source Converters**

Gholami-Khesht, Hosein; Davari, Pooya; Wu, Chao; Blaabjerg, Frede

*Published in:*  
Applied Sciences

*DOI (link to publication from Publisher):*  
[10.3390/app12178893](https://doi.org/10.3390/app12178893)

*Creative Commons License*  
CC BY 4.0

*Publication date:*  
2022

*Document Version*  
Publisher's PDF, also known as Version of record

[Link to publication from Aalborg University](#)

*Citation for published version (APA):*  
Gholami-Khesht, H., Davari, P., Wu, C., & Blaabjerg, F. (2022). A Systematic Control Design Method with Active Damping Control in Voltage Source Converters. *Applied Sciences*, 12(17), Article 8893.  
<https://doi.org/10.3390/app12178893>

### **General rights**

Copyright and moral rights for the publications made accessible in the public portal are retained by the authors and/or other copyright owners and it is a condition of accessing publications that users recognise and abide by the legal requirements associated with these rights.



- Users may download and print one copy of any publication from the public portal for the purpose of private study or research.
- You may not further distribute the material or use it for any profit-making activity or commercial gain
- You may freely distribute the URL identifying the publication in the public portal -

### **Take down policy**

If you believe that this document breaches copyright please contact us at [vbn@aub.aau.dk](mailto:vbn@aub.aau.dk) providing details, and we will remove access to the work immediately and investigate your claim.

## Article

# A Systematic Control Design Method with Active Damping Control in Voltage Source Converters

Hosein Gholami-Khesht<sup>1</sup>, Pooya Davari<sup>1,\*</sup>, Chao Wu<sup>2</sup> and Frede Blaabjerg<sup>1</sup><sup>1</sup> AAU Energy, Aalborg University, 9220 Aalborg, Denmark<sup>2</sup> Department of Electrical Engineering, Shanghai Jiao Tong University, Shanghai 200240, China

\* Correspondence: pda@energy.aau.dk

**Abstract:** This paper proposes a systematic control design method for active damping control of grid-connected voltage source converters (VSCs). The proposed control method considers the conventional cascaded control loops and improves them by including additional states feedback-based active damping. In such a way, all control gains are lumped into one control gain matrix based on the proposed formulation. The lumping of all control gains into one matrix leads to a linear optimization problem, so different techniques can be used to calculate control gains. This work calculates them by using a simple but effective optimal control theorem as a noteworthy feature. The proposed control method can overcome the challenges of designing multiple control loops, evaluating wide time scale dynamics, and tuning required control parameters. Moreover, direct relationships between the proposed tuning parameters and system well-known stability and performance indicators such as maximum damping factor, minimum damping ratio, and the control efforts are identified, providing good physical insight. Finally, the proposed control structure and optimal gain calculations ensure power converter robustness against uncertainties in the grid's short-circuit ratio (SCR) and different operating-point conditions. When the grid's SCR changes from 10 (strong grid condition) to 1 (ultra-weak grid condition), the system under the proposed control method maintains good stability margins and simultaneously provides a fast dynamic response by facilitating the implementation of a high-bandwidth phase-locked loop (PLL). The performance of the proposed control strategy was investigated analytically and practically by conducting eigenvalue analysis, simulations, and experiments.

**Keywords:** voltage source converters (VSCs); grid-connected VSC; weak grids; robustness analysis; optimal-state feedback control



**Citation:** Gholami-Khesht, H.; Davari, P.; Wu, C.; Blaabjerg, F. A Systematic Control Design Method with Active Damping Control in Voltage Source Converters. *Appl. Sci.* **2022**, *12*, 8893. <https://doi.org/10.3390/app12178893>

Academic Editor: Giovanni Petrone

Received: 15 July 2022

Accepted: 30 August 2022

Published: 5 September 2022

**Publisher's Note:** MDPI stays neutral with regard to jurisdictional claims in published maps and institutional affiliations.



**Copyright:** © 2022 by the authors. Licensee MDPI, Basel, Switzerland. This article is an open access article distributed under the terms and conditions of the Creative Commons Attribution (CC BY) license (<https://creativecommons.org/licenses/by/4.0/>).

## 1. Introduction

Grid-connected voltage source converters (VSCs) have become one of the main components of the modern power system due to their fast dynamic response, full controllability, and flexibility. They can be found in many power-system applications such as renewable-energy-based generation (wind turbines (WT) and photovoltaic (PV) power plants), electric power transmission systems, and load and power quality equipment. Multiple control loops are employed in the control of VSCs to improve the performance, including active power control loop or dc-link voltage controller (DVC), reactive power control loop or ac voltage magnitude controller (AVC), inverter current control loop (CC) and protection, voltage feedforward controller (VFF) to damp LCL filter resonances, and a phase-locked loop (PLL) for grid synchronization. However, it has been revealed that these control loops are strongly coupled and lead to complex, asymmetric, and wide timescale dynamics. Therefore, an inaccurate control loop design and the possible interaction among different control loops may cause performance degradation or even system instability [1–4]. These stability concerns become more severe under weak grids, where the power grid at the

connection point has a lower short circuit ratio (SCR) due to the high penetration level of power converters or long distance between distributed generators and the main grid.

Many efforts have been made to present more efficient design strategies and enhance the control system's performance by including additional active damping terms to address the mentioned problems. Conventional design strategies such as the generalized Nyquist theorem or passivity theorem are based on the impedance model to investigate the system's stability and control-parameter selection [5,6]. For instance, in Reference [7], a recursive adjustment procedure for the current controller's gains is suggested based on the frequency response. This work considers only the control delay effect. A comprehensive stability analysis and the current control design of a grid-connected LCL-filtered VSC are discussed in Reference [8]. To damp the LCL filter resonances and the negative impact of the control delay, a grid-side current control-based active damping and virtual flux-based active damping are proposed in References [9,10], respectively. Moreover, to limit the negative impact of digital filters (commonly used in the CC and VFF) on the dissipativity of the output converter admittance, some design guidelines are proposed by Reference [11]. However, calculating the impedance model and performing a stability analysis are challenging and require high expertise and physical insight. Moreover, designing a control system and selecting the optimal values of the control parameters are not trivial tasks, especially for a high-order multi-input, multi-output (MIMO) system such as grid-connected VSCs. Therefore, the control gain selection is generally an iterative process.

A full state-space feedback control method to improve the resonance damping of the LCL filter and increase the system robustness against the grid SCR variations is presented in References [12,13]. The proportional-integral (PI) current control and active damping gains in Reference [12] are calculated by using the pole placement technique. Despite the simplicity in concept, selecting the desired closed-loop poles is a challenging task; it becomes more difficult or even impossible for a high-order MIMO system. A systematic design procedure based on the optimal control theorem is suggested in Reference [13] to avoid direct pole placement. However, weighting factors' selection is required [13,14].

In References [15–19], a robust proportional-resonant (PR) current control design based on the H-infinity theorem and linear matrix inequalities (LMIs) is proposed to consider the impact of the grid SCR variations in the design procedure. However, the optimal robust H-infinity control leads to high control gains, making some difficulties for practical implementation [15,16,18].

Although the previous works provide valuable results, they did not consider the impact of PLL and outer control loops. Therefore, they suffer from some conservatism in their design. Moreover, active damping based on the feedforward PCC voltage or current feedback, which is widely suggested, is only efficient to damp oscillations in the LCL filter resonance range and not low-frequency oscillations due to the outer control loops interaction.

In Reference [20], a state feedback-based active damping control to dampen low-frequency oscillations is proposed. However, a low-order and simplified model is considered for the fast dynamics parts (LCL filter, delay, and current controller) to simplify the control system design. Moreover, it suffers from shortcomings of the pole-placement techniques and recursive process. Finally, the possibility of implementing a high-performance PLL in weak grids was not discussed.

Research work in Reference [21] introduced an improved current control design to reduce the negative impact of the PLL on the current controller in weak grids, which need extra capacitor current sensors.

In Reference [22], an optimal control method is proposed to enhance the inner current control loop performance and reduce the negative impact of PLL in weak grids. However, many weighting factors are added to the design procedure, transparent relationships between tuning parameters and stability and performance indicators (e.g., damping factor and ratio) are not identified, and the outer control loops are not considered.

The authors of Reference [23] presented a loop-at-a-time stability analysis (LAAT), and based on LAAT, a design algorithm for outer control loops (DVC and AVC) is also suggested. The proposed method is closely correlated to the characteristic loci in the generalized Nyquist criterion for MIMO systems and tries to overcome challenges regarding the MIMO control system design in the frequency domain. However, to reduce the complexity of the method, the inner current control loop and PLL are embedded inside the plant.

In Reference [24], a fixed-structure H-infinity control design is presented to calculate the outer loops' control gains. However, the design procedure needs dynamic weighting function calculations for each input and output relation. In this regard, many parameters are required to be tuned, significantly affecting the system response and feasibility of the H-infinity optimization problem.

Overall, the prior state-of-the-art methods mentioned above partially address grid uncertainties, low and high-frequency oscillations, control loops interaction, high-order MIMO structure, and recursive control system design. However, none of them succeeds in presenting a comprehensive and efficient solution, as summarized in Table 1. For example, all previous works consider only inner or outer control loops and ignore the other ones in the design step. When all control loops are considered simultaneously, the couplings of some inner and outer control parameters have appeared, leading to a nonlinear system and optimization problem.

**Table 1.** State-of-the-art control-system design techniques.

References	Design Technique	Inner Control Loops Design	Outer Control Loops Design	PLL Impact	Weak Grid Conditions	Extra Current Sensors	Expertise to Design	Optimizing Control Efforts	Applicability to MIMO Systems
[7]	Nyquist	yes	no	no	no	no	medium	no	hard
[8]	Nyquist	yes	no	no	yes	no	medium	no	hard
[12]	Full state feedback	yes	no	no	yes	yes	low	no	medium
[13]	Optimal control	yes	no	no	no	yes	medium	yes	easy
[22]	Optimal control	yes	no	yes	yes	yes	medium	yes	easy
[15–17]	Robust H-infinity	yes	no	no	no	yes	high	yes	medium
[19]	Robust H-infinity	yes	no	no	yes	yes	high	yes	medium
[23]	loop-at-a-time	no	yes	no	yes	no	high	no	medium
[24]	Robust H-infinity	no	yes	yes	yes	yes	high	yes	medium
Proposed	Optimal control	yes	yes	yes	yes	no	medium	yes	easy

In this respect, this paper tries to propose a new systematic design approach in order to simplify the control gains calculation by providing a linear optimization problem. Based on the new formulation, all control gains are lumped into one control gain matrix, and then different techniques can be used to calculate the system control gain matrix. Among others, this work employs the linear-quadratic regulator (LQR) design framework due to its efficiency and applicability.

The main contributions of this paper are listed as follows:

- Proposing a direct design approach with the minimum recursive process to calculate the control parameters,
- Providing a clear insight between tuning parameters and stability and performance indicators,

- Increasing system robustness against uncertainties in the grid impedance and operating point conditions,
- Improving system transient response and fault ride-through (FRT) capability by implementing a PLL with higher bandwidths.

The remainder of this paper is organized as follows. Section 2 describes the under-studied system, a grid-connected LCL-filtered VSC with all control loops. The proposed nonlinear and linearized dynamics of a grid-connected VSC are also presented in this section. The proposed robust and optimal active damping control is introduced in Section 3. Furthermore, some guidelines for selecting the state and input weighting matrixes are provided. This section is completed with a comprehensive robustness analysis based on the eigenvalue analysis to consider the impact of different grid SCRs and operating point conditions. A comparison with the conventional one is also given. The analytical results were verified by several simulations and experimental tests under different operational conditions, as recounted in Section 4. Finally, Section 5 concludes this paper.

## 2. System Description and Modeling

Figure 1 shows the principal scheme of the studied system, which includes primary energy sources (i.e., the solar power plant or the wind turbine systems), the power grid, back-to-back three-phase voltage source converter (VSC), an LCL output filter, and a control system. The power grid is represented by a Thevenin model seen from the point of common coupling (PCC).

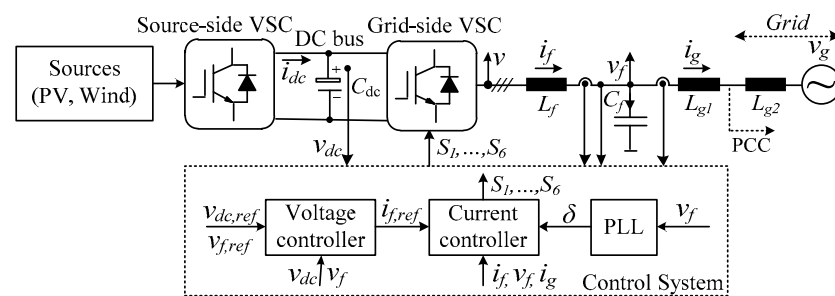


**Figure 1.** Single line diagram of an LCL-filtered grid-connected three-phase voltage source converter (VSC).

The grid inductance ( $L_{g2}$ ) can also vary widely to mimic a weaker or stronger connection point. The remaining parameters in Figure 1 are as follows:  $i_f$ ,  $i_g$ ,  $v_f$ ,  $v$ ,  $v_g$ ,  $v_{dc}$ , and  $i_{dc}$  are the converter and grid currents, voltage across the filter capacitor, inverter and grid voltages, dc-link voltage, and dc-side current, respectively. Moreover,  $L_f$ ,  $L_{g1}$ ,  $C_f$ ,  $L_{g2}$ , and  $C_{dc}$  represent the converter and grid-side filter inductances, filter capacitance, equivalent grid inductance, and dc-link capacitance, respectively;  $\delta$  is the phase angle obtained by the PLL; and the subscript *ref* gives the reference values for different control loops.

### 2.1. Derivation of Proposed Control Method

The main aims of the grid-side VSC are to inject the produced power by renewable energy systems into the power grid with the sinusoidal current. However, the voltage compensation of the PCC is also necessary when connected to a weak grid.

The conventional control systems of grid-side VSC are shown in Figure 2. The conventional one consists of five main parts, including the dc-link voltage controller (DVC), AC voltage magnitude controller (AVC), current controller (CC), voltage feedforward controller (VFF), and a synchronous reference frame phase-locked loop (SRF-PLL). It is worth remarking that they all (except for VFF) employ a proportional-integral (PI) controller to ensure good dynamic response and zero steady-state tracking error in the synchronous reference frame. Moreover, grid-side current feedback and voltage feedforward control through a high-pass filter are provided to damp the LCL filter resonances and better disturbance

rejection. In this work, a first-order high-pass filter is considered for VFF, which is expressed as follows [25]:

$$VFF = \frac{k_a s}{s + \omega_a} \tag{1}$$

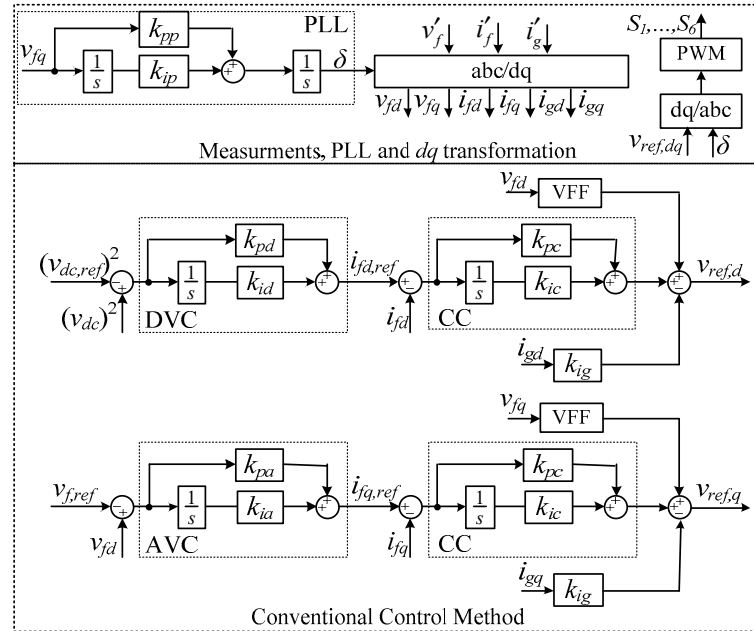


**Figure 2.** The conventional control method. VFF, voltage feedforward controller; DVC, dc-link voltage controller; AVC, ac voltage-magnitude controller; CC, current controller; PLL, phase-locked loop.

As it can be seen, the conventional structure employs many control loops with at least eleven control gains which should be designed carefully to provide a proper response and stability margins and also avoid control loops’ interactions. Moreover, there are many states in the system that can be appropriately utilized. It seems proper that employing them may remarkably increase the system’s robustness and performance, as shown in Figure 3. Here,  $K_f$  and  $x$  are the active damping gain matrix and system state’s vector, respectively. However, it may add extra feedback gains and increase complexity to calculate the optimal control gains.

The control structure in Figure 3 can be simplified as follows. Since  $k_{pd}$  and  $K_{f1}(1,15)$  are multiplied by  $\Delta v_{dc}$  and provide the same damping, one can be ignored to reduce the number of tuning parameters. The same can also be concluded for CC, AVC, and integral gains. The resultant simplified control structure is depicted in Figure 4.

By comparing Figures 3 and 4, it can be seen that duplicate coefficients are ignored, and all control gains of different control loops and state feedback-based active damping are lumped in the control gain matrix ( $K_f$ ).

Therefore, the proposed control method can utilize the maximum capability of the circuit and control systems and employs all available states ( $x$ ) to improve the system’s response.

Moreover, a high-pass filter-based VFF, which is necessary to damp LCL filter responses under weak grid conditions, is also replaced with the simpler constant feedback controller. It is shown here that, although a dynamic controller is not considered for the VFF, the proposed control structure can still provide better robustness under weak grid conditions, as another noteworthy feature.

The remaining question is how the control gain matrix can be obtained and based on which criteria. In the following, at first, a proper representation of the system equations is provided. Then, based on the proposed system model, a design procedure is presented to obtain the control gain matrix optimally and simply.

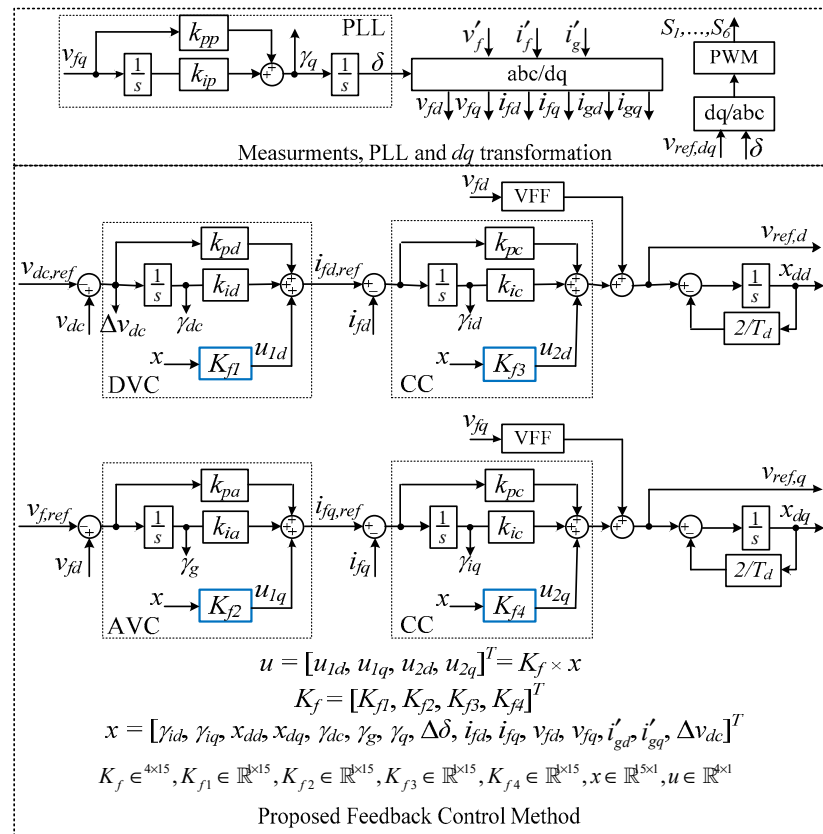


Figure 3. The proposed solution is to include state-feedback-based active damping in the inner and outer control loops.

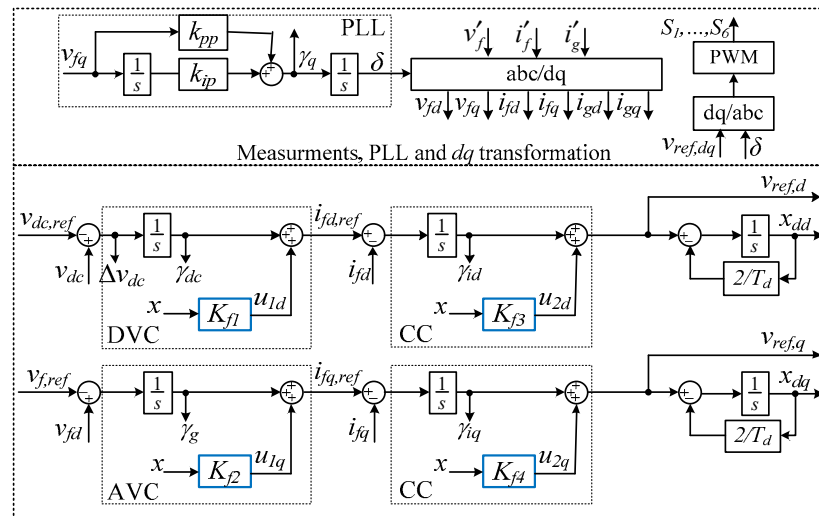


Figure 4. The proposed control method.

2.2. Proposed Nonlinear and Linearized State-Space Model of a Grid-Connected VSC for Optimal Control System Design

Considering the active power-balance equation, Park transformation, and control delay in the digital implementation in Figures 1 and 4, the proposed state-space nonlinear model of the overall system is determined as follows:

$$\begin{aligned}
 \dot{\gamma}_q &= v_{fq} \\
 \dot{\delta} &= k_{pp}v_{fq} + k_{ip}\gamma_q \\
 \dot{\gamma}_{dc} &= v_{dc,ref} - v_{dc} \\
 \dot{\gamma}_g &= v_{f,ref} - v_{fd} \\
 \dot{\gamma}_{id} &= -\gamma_{dc} - i_{fd} + u_{1d} \\
 \dot{\gamma}_{iq} &= -\gamma_g - i_{fq} + u_{1q} \\
 v_{ref,d} &= \gamma_{id} + u_{2d} \\
 v_{ref,q} &= \gamma_{iq} + u_{2q} \\
 \dot{x}_{dd} &= (-2/T_d)x_{dd} + v_{ref,d} \\
 \dot{x}_{dq} &= (-2/T_d)x_{dq} + v_{ref,q} \\
 v_d &= (4/T_d)x_{dd} - v_{ref,d} \\
 v_q &= (4/T_d)x_{dq} - v_{ref,q} \\
 i_{fd} &= L_1^{-1} \left( L_1\omega_1 i_{fq} + v_d - v_{fd} \right) \\
 i_{fq} &= L_1^{-1} \left( -L_1\omega_1 i_{fd} + v_q - v_{fq} \right) \\
 \dot{v}_{fd} &= C_f^{-1} \left( C_f\omega_1 v_{fq} + i_{fd} - \cos(\delta) i'_{gd} - \sin(\delta) i'_{gq} \right) \\
 \dot{v}_{fq} &= C_f^{-1} \left( -C_f\omega_1 v_{fd} + i_{fq} + \sin(\delta) i'_{gd} - \cos(\delta) i'_{gq} \right) \\
 i'_{gd} &= L_g^{-1} \left( L_g\omega_1 i'_g + \cos(\delta) v_{fd} - \sin(\delta) v_{fq} - v'_{gd} \right) \\
 i'_{gq} &= L_g^{-1} \left( -L_g\omega_1 i'_g + \sin(\delta) v_{fd} + \cos(\delta) v_{fq} - v'_{gq} \right) \\
 \dot{v}_{dc} &= \frac{-1}{C_{dc}} \frac{v_{fd} \cdot i_{fd} + v_{fq} \cdot i_{fq}}{v_{dc}} + \frac{1}{C_{dc}} i_{dc}
 \end{aligned} \tag{2}$$

where  $L_g = L_{g1} + L_{g2}$ , and  $\gamma_q, \gamma_{dc}, \gamma_g, \gamma_{id}$ , and  $\gamma_{iq}$  are integral states for the PLL, DVC, AVC, and current controller (CC), respectively. It is worth noting that the converter is assumed to be lossless, and the delay is approximated by the following transfer function, using first-order Pade approximation [26]:

$$\frac{v}{v_{ref}} = e^{(-T_d s)} \approx \frac{2 - T_d s}{2 + T_d s} \rightarrow \begin{cases} \dot{x}_d = (-2/T_d)x_d + v_{ref} \\ v = (4/T_d)x_d - v_{ref} \end{cases} \tag{3}$$

Furthermore, two  $dq$ -frames are considered to include the impact of PLL in the system model and analysis. The global  $dq$ -frame is aligned with the infinite bus voltage, and the converter or local  $dq$ -frame is aligned with the PCC voltage. Signals in the global and the converter  $dq$  frames are represented with and without the apostrophe superscript ( $'$ ), respectively [27].

The nonlinear model can be rewritten in the following compact form:

$$\dot{x} = f(x, u, d) \tag{4}$$

Here the system state ( $x$ ) and the control and disturbance inputs ( $u$  and  $d$ ) are as follows:

$$\begin{aligned}
 x &= \left[ \gamma_{id} \quad \gamma_{iq} \quad x_{dd} \quad x_{dq} \quad \gamma_{dc} \quad \gamma_g \quad \gamma_q \quad \delta \quad i_{fd} \quad i_{fq} \quad v_{fd} \quad v_{fq} \quad i'_{gd} \quad i'_{gq} \quad \Delta v_{dc} \right]^T \\
 u &= \left[ u_{1d} \quad u_{1q} \quad u_{2d} \quad u_{2q} \right]^T, \quad d = \left[ v_{dc,ref} \quad v_{f,ref} \quad v'_g \quad i_{dc} \right]^T
 \end{aligned} \tag{5}$$



A linearized state-space model around an equilibrium point ( $x_e, u_e$ , and  $d_e$ ) is required, which facilitates designing a state feedback control for a grid-connected VSC. The following equations can be used to calculate the linearized model:

$$\dot{x} = Ax + Bu + Dd \tag{6}$$

$$\begin{aligned} A &= \left. \frac{\partial f}{\partial x} \right|_{x=x_e, u=u_e, d=d_e} \\ B &= \left. \frac{\partial f}{\partial u} \right|_{x=x_e, u=u_e, d=d_e} \\ D &= \left. \frac{\partial f}{\partial d} \right|_{x=x_e, u=u_e, d=d_e} \end{aligned} \tag{7}$$

### 3. Design of the Control Gain Matrix

In the existing literature [12–19], it is evident that using more states in the control structure is better for the dynamic performance and stability margin under a weak grid. However, how to design the control gain matrix is an unsolved question. This section presents a linear-quadratic regulator (LQR) design framework to achieve an optimal, robust, and multivariable control of grid-connected VSCs.

Given the system dynamics in (6), the static full-state-feedback law is as follows:

$$u = -K_f x \tag{8}$$

The optimal gain matrix,  $K_f$ , is calculated to minimize the following infinite-horizon quadratic cost function:

$$J(u) = \int_0^\infty (x^T Q x + u^T R u) dt, Q = Q^T \geq 0, R = R^T \geq 0 \tag{9}$$

where  $Q$  and  $R$  are constant weighting matrixes that set relative weights of state deviation and input usage; the optimal gain matrix is given by the following:

$$K_f = R^{-1} B^T P \tag{10}$$

where the positive definite matrix,  $P$ , is a solution of the following algebraic Riccati equation:

$$A^T P + PA - PBR^{-1}B^T P + Q = 0 \tag{11}$$

The solution leads to a stable closed-loop transfer function ( $A_{cl} = A - BK_f$ ) and minimizes the defined performance quadratic cost function ( $J$ ). Furthermore, it is well-known that the equation has a single positive-definite solution if, and only if, the pairs of  $(A, B)$  and  $(\sqrt{Q}, A)$  are stabilizable and detectable, respectively. Moreover, there are suitable numerical methods to find the solution, even for MIMO systems or high-dimensional problems.

#### 3.1. Weighting Matrixes' Selection

As the previous subsection can conclude, the optimal state-feedback control design of grid-connected VSC is reduced to the proper choice of weighting matrixes ( $Q$  and  $R$ ). Bryson's rule can be used to select weighting matrixes as a primary choice. Moreover, References [28,29] have provided some guidelines to choose weighting matrixes. For instance, a procedure based on minimizing the infinity norm of selected transfer functions is suggested in Reference [29]. However, there are two main issues for the understudied system that should be appropriately answered: (1) Is it possible to reduce the number of tuning parameters? ( $Q$  and  $R$  have 130 elements to tune.) (2) Can physical meaning be provided for them, and how can they be related to well-known system stability and performance indicators such as the maximum damping factor ( $\sigma_{max}$ ) and minimum damping ratio ( $\xi_{min}$ )?

Many recommendations for properly tuning weighting matrixes in general and, after that, for the specific understudied system are presented in this section. For simplicity in tuning, diagonal matrixes are usually selected. It is worth remarking that the diagonal elements of weighting matrixes ( $q_i$  or  $r_i$ ) are the maximum expected or acceptable value of the related state  $(x_i^2)^{-1}$  or input  $(u_i^2)^{-1}$ . A higher  $Q$  results in a smaller steady-state error, higher bandwidth, faster dynamic response, and better disturbance rejection. However, it causes higher sensitivity to noise and unmodeled dynamics and increases the norm of control gain matrix, leading to chattering and control input saturation. Therefore, the selection of  $Q$  and  $R$  compromises a fast dynamic response, adequate stability margin, and acceptable control matrix norm. The compromised values can be obtained systematically with a simple computer-aided program. For example, for different values of weighting matrixes, the damping factor and damping ratio of the critical mode and the norm of the control gain matrix ( $\text{norm}(K_f) = \|K_f\|$ ) are calculated. Then the stability and performance criteria are checked. If the desired performance is fulfilled, the process is stopped; otherwise, proper actions should be taken.

Although the previous process can also find proper weighting factors, nineteen tuning parameters (fifteen parameters in  $Q$  and four in the  $R$ ) should be selected, which increases the design process time. Therefore, further reduction of the number of individual tuning parameters is still desirable. Moreover, physical inspiration about their impact is not presented yet. Thus, a more detailed discussion on the weighting factors tuning for the understudied system is presented as follows.

Since there are four control inputs ( $u_{1d}$ ,  $u_{1q}$ ,  $u_{2d}$ , and  $u_{2q}$ ) and three important stability and performance indicators ( $\sigma_{max}$ ,  $\xi_{min}$ , and  $\text{norm}(K_f)$ ), three or four individual parameters in the weighting matrixes may provide the requirements mentioned above.

Therefore, the following suggestions are provided.

First, the input cost matrix is selected as  $R = rI_{4 \times 4}$ ; therefore, only one  $r$  is needed to be chosen. Moreover, the different characteristics of the states can be divided into three different groups: integrals of the tracking errors ( $\gamma_{id}$ ,  $\gamma_{iq}$ ,  $\gamma_{dc}$ ,  $\gamma_g$ ,  $\gamma_q$ ), dc-link voltage tracking error ( $\Delta v_{dc}$ ), and the remaining states ( $x_{dd}$ ,  $x_{dq}$ ,  $\delta$ ,  $i_{fd}$ ,  $i_{fq}$ ,  $v_{fd}$ ,  $v_{fq}$ ,  $i'_{gd}$ ,  $i'_{gq}$ ).

For the first group, these states are directly related to the control errors, which represent the steady-state error. For the second group, it can affect the transient response of dc-link voltage tracking error and, consequently, inverter current. For the last one, the states are just intermediate states which are directly related to the control performance. Based on the classification of the states, the states' cost matrix is selected as  $Q = \text{diag}(q_1, q_1, q_2, q_2, q_1, q_1, q_1, q_2, q_2, q_2, q_2, q_2, q_2, q_3)$ .

First, stability and performance definitions are provided. Then the impact of different values of tuning parameters ( $q_1$ ,  $q_2$ ,  $q_3$ , and  $r$ ) on the system stability and performance and the control gain matrix are studied. The results are summarized in Table 2.

**Table 2.** Impact of tuning parameters ( $q_1$ ,  $q_2$ ,  $q_3$ , and  $r$ ) on the control gain matrix and the system stability and performance.

$q_1$	$\text{norm}(K_f)$	$\sigma_{max}$	$\xi_{min}$	$q_2$	$\text{norm}(K_f)$	$\sigma_{max}$	$\xi_{min}$
$1 \times 10^1$	$9.7 \times 10^3$	-1.5	0.28	$1 \times 10^{-2}$	$1.6 \times 10^3$	-42	0.03
$1 \times 10^2$	$9.8 \times 10^3$	-4.5	0.28	$1 \times 10^{-1}$	$3.5 \times 10^3$	-41.9	0.1
$1 \times 10^3$	$9.8 \times 10^3$	-14.1	0.28	$5 \times 10^{-1}$	$7.1 \times 10^3$	-41.8	0.21
$1 \times 10^4$	$9.9 \times 10^3$	-41.6	0.28	1	$9.8 \times 10^3$	-41.6	0.28
$2 \times 10^4$	$9.9 \times 10^3$	-41.2	0.28	2	$13.8 \times 10^3$	-41.1	0.36
$1 \times 10^5$	$10.2 \times 10^3$	-41	0.28	5	$21.5 \times 10^3$	-34	0.39
$1 \times 10^6$	$11.3 \times 10^3$	-41	0.28	10	$29.8 \times 10^3$	-26	0.42

**Table 2.** Cont.

$q_3$	$\text{norm}(K_f)$	$\sigma_{max}$	$\zeta_{min}$	$R$	$\text{norm}(K_f)$	$\sigma_{max}$	$\zeta_{min}$
$1 \times 10^{-2}$	$9.7 \times 10^3$	-40	0.26	$1 \times 10^{-2}$	$99.3 \times 10^3$	-42	0.48
$1 \times 10^{-1}$	$9.7 \times 10^3$	-40	0.27	$1 \times 10^{-1}$	$36.5 \times 10^3$	-42	0.47
1	$9.7 \times 10^3$	-40	0.28	1	$12.1 \times 10^3$	-42	0.32
2	$9.8 \times 10^3$	-40	0.28	2	$8.5 \times 10^3$	-41	0.25
5	$9.9 \times 10^3$	-42	0.28	5	$5.3 \times 10^3$	-31	0.17
10	$10 \times 10^3$	-31	0.28	10	$3.8 \times 10^3$	-23	0.12
100	$10.7 \times 10^3$	-10	0.28	100	$1.3 \times 10^3$	-7	0.03

*Definitions, stability, and performance indicators:*

The following equations can represent the  $i$ th eigenvalue of the system ( $\lambda_i$ ) and its damping factor ( $\sigma_i$ ), frequency of oscillations ( $\omega_{di}$ ), and damping ratio ( $\zeta_i$ ):

$$\lambda_i = \sigma_i \pm j\omega_{di}, \zeta_i = \frac{-\sigma_i}{\sqrt{\sigma_i^2 + \omega_{di}^2}} \tag{12}$$

It is worth remarking that the system is stable for  $\sigma < 0$  and  $\zeta > 0$ , oscillating for  $\sigma = \zeta = 0$ , and unstable for  $\sigma > 0$  and  $\zeta < 0$ . The unstable or weakest damped eigenvalue among all eigenvalues, called a critical mode, causes significant oscillations or even system instability. To guarantee stability margin and limit the system overshoot, the damping factor and ratio of the critical mode should fulfill some requirements ( $\sigma \leq \sigma_{min\_max}$ ). The desired damping ratio depends on the modal frequency and accepted oscillation settling time by different utilities and standards [30,31]. It is usually selected to be something between 5 and 20 percent. In this work, a desired 10% damping ratio is accepted, guaranteeing an acceptable overshoot and decay rate of oscillations. Moreover, placing the maximum damping factor far from the imaginary axis can ensure system stability and improve response speed in terms of the rise time. The system’s rise time is assigned by the outer voltage control loops that have lower bandwidths among different control loops. For example, a rise time ( $t_r$ ) lower than 100 ms is usually required for AVC, resulting in a maximum damping factor less than 22 rad/s: ( $\sigma_{max} \approx -2.2/t_r = -2.2/100 \text{ ms} = -22 \text{ rad/s}$ ) [23].

*Selection of  $q_1$ :*

As it can be seen in Table 2, this parameter has a significant impact on the maximum damping factor. For example, for  $q_1 = 10$ , the system is close to the imaginary axis and hazardous area ( $\sigma_{max} = -1.5 \text{ rad/s}$ ). By increasing this parameter to  $q_1 = 1 \times 10^4$ , the critical mode moves far from the imaginary axis to obtain a good stability margin ( $\sigma_{max} = -40 \text{ rad/s}$ ). However, by increasing the  $q_1$  more, the critical mode is not changed anymore, while the control gain norm increases. Thus, at this point, if the obtained damping factor is acceptable,  $q_1$  can be used for the control gain calculation in (10). Otherwise, the new initial values for all tuning parameters should be selected, and the process should be repeated.

A good decision is to set a lower value for  $r$  to allow more control input usage. This action may provide a better stability margin in terms of the damping factor. Finally, as it can be seen, the damping ratio is not affected, and it remained constant for different values of  $q_1$ .

*Selection of  $q_2$ :*

Unlike the  $q_1$ ,  $q_2$  does not affect the damping factor, while it affects the damping ratio considerably. For a lower value, the  $\zeta_{min}$  is close to zero, which is undesirable and causes higher overshoots. Increasing this parameter increases the system damping ratio remarkably in the cost of higher control gains. Therefore, the selection of this parameter is a compromise between damping ratio and control gains norm.

Selection of  $q_3$ :

Overall,  $q_3$  has a significant impact on the tracking error of dc-link voltage. A higher  $q_3$  causes the faster tracking of dc-link voltage at the price of higher overshoot in the inverter current. The inverter current (especially  $d$ -axis current) acts as a control input for DVC. Therefore, it can be expected that the faster convergence rate of the dc-link voltage may lead to more current variations and overshoots. Inverter overcurrent protection limits the current overshoot. Thus, there is also a compromise here that  $q_3$  can obtain.

Figure 5 shows system response for two different values of  $q_3$ . For a higher value, dc-link voltage tracks the reference one quickly and without oscillations at the expense of the higher current overshoot and vice versa.

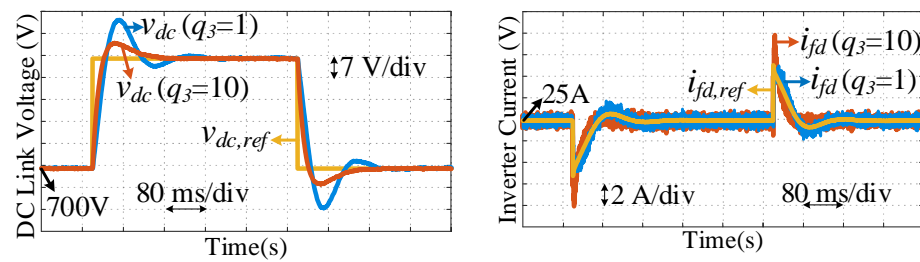


**Figure 5.** Impacts of tuning parameter  $q_3$  on the system outputs ( $q_1 = 1 \times 10^4$ ,  $q_2 = 1$ , and  $r = 1.5$ ), ( $q_3 = 1$ , norm ( $K$ ) =  $9.7 \times 10^3$ ,  $\sigma_{max} = -39$ , and  $\zeta_{min} = 0.28$ ) in blue, and ( $q_3 = 10$ , norm ( $K$ ) =  $9.9 \times 10^3$ ,  $\sigma_{max} = -31$ , and  $\zeta_{min} = 0.28$ ) in orange.

Selection of  $r$ :

This parameter affects the norm of the control gain matrix. Lower values mean permission for higher control gains and vice versa. As expected, and as seen in Table 2, for the lower value of  $r$ , the stability and performance indicators are superior, but the norm of the control gain matrix is high. High control gains cause many difficulties for practical implementation and increase the sensitivity to noise and time delay. Figure 6 shows the system output for two different norm values of the control gain matrix. For the higher one, chattering and oscillations in outputs are seen. By increasing  $r$  and reducing the norm of the control gain matrix, these oscillations disappear.

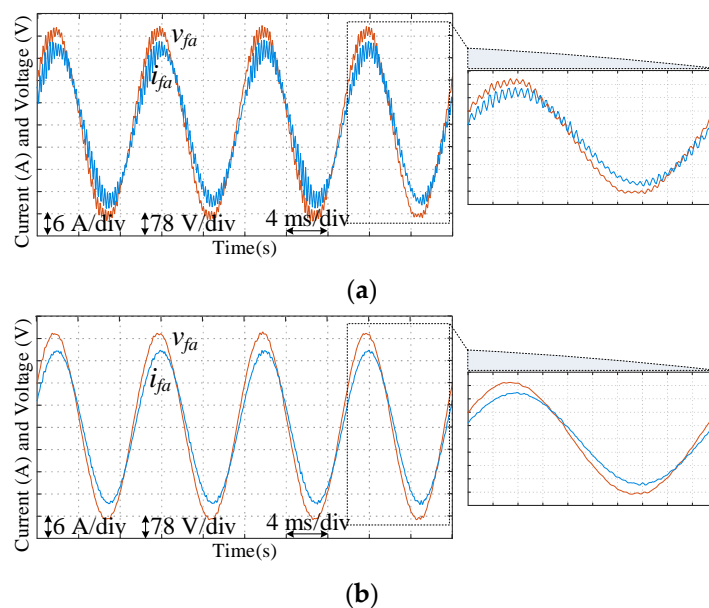


**Figure 6.** Impacts of tuning parameter  $r$  and norm of control gain matrix ( $K$ ) on the system outputs ( $q_1 = 1 \times 10^4$ ,  $q_2 = 1$ , and  $q_3 = 5$ ): (a) ( $r = 0.5$ , norm ( $K$ ) =  $1.7 \times 10^4$ ,  $\sigma_{max} = -41$ , and  $\zeta_{min} = 0.4$ ) and (b) ( $r = 1.5$ , norm ( $K$ ) =  $9.1 \times 10^3$ ,  $\sigma_{max} = -41$ , and  $\zeta_{min} = 0.28$ ).

*A summary of the weighting factors design procedure:*

As shown so far, in the proposed design algorithm, an almost direct relation between tuning parameters and desired stability and performance requirements is identified that considerably simplifies the control system’s design.

In such a way, by adjusting  $q_1$ ,  $q_2$ ,  $r$ , and  $q_3$ , the desired maximum damping factor, minimum damping ratio, control gain matrix norm, and transient response are obtained.

Hence, the design process can be summarized as follows:

- Step 1: Small values for  $q_1$ ,  $q_2$ ,  $q_3$ , and  $r$  are selected.
- Step 2: Increasing  $q_1$  adjusts the maximum damping factor.
- Step 3: Increasing  $q_2$  adjusts the minimum damping ratio.
- Step 4: Increasing  $r$  reduces control gain matrix norm.
- Step 5: Increasing  $q_3$  changes dc-link voltage and inverter current transient response.

As it can be seen, the design procedure is very straightforward, and repetitive actions are reduced considerably.

**3.2. Robustness Analysis**

The previous design process can provide sufficient stability margins. However, these excellent stability margins are guaranteed for the nominal values of system parameters. However, some of these parameters may not be constant during the inverter operation. For example, their operating-point conditions continuously change during the day, and the grid SCR can vary over a wide range due to variations of the connected load and generators.

In this respect, a robustness assessment based on the eigenvalue calculation was carried out to examine the system’s robustness under these uncertainties. In such a way, the variations in the critical mode are studied for different values of grid SCR and operating point conditions. In addition, a comparison between the proposed and the conventional control methods is also given.

The stability margins of the proposed control method are calculated based on the linearized model in (6) and feedback control gain in (10) ( $A_{cl} = A - BK_f$ ). It is worth remarking that the control gain matrix in (10) is calculated for the nominal power ( $P_n$ ), the average value of grid SCR (SCR = 5.5), and  $f_{PLL} = 10$  Hz. Then the control gain matrix is kept constant during the robustness assessment. Moreover, the critical mode of a conventional control system, as shown in Figure 2, is determined based on the linearized model represented in Reference [25]. Therefore, it is not repeated, and the interested reader can refer to it for more details.

Figure 7 investigates the impact of grid SCR uncertainties ( $1 < SCR < 10$ ), different PLL bandwidths ( $8 \text{ Hz} < f_{PLL} < 80 \text{ Hz}$ ), and inverter power levels ( $0.01 P_n < P < P_n$ ) on the critical mode under both proposed and conventional control methods. The following conclusions can be drawn from this figure:

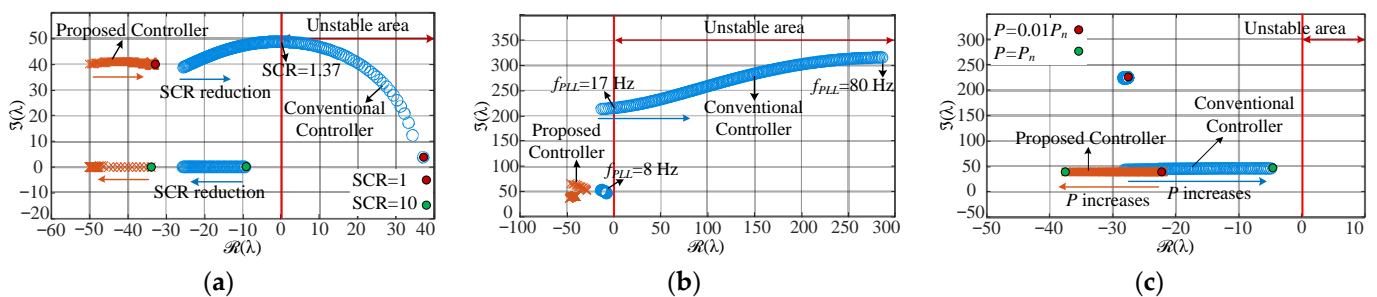


**Figure 7.** Critical mode locations of a grid-connected VSC in the complex s-plane: (a) impact of grid SCR variations  $P = P_n$ ,  $f_{PLL} = 10$  Hz (conventional controller), and 50 Hz (proposed controller); (b) impact of different PLL bandwidths ( $P = P_n$ , SCR = 1.5); and (c) impact of inverter power level SCR = 1.5,  $f_{PLL} = 10$  Hz (conventional controller), and 50 Hz (proposed controller).

(1) In Figure 7a, the grid SCR varies from 10 (strong grid condition) to 1 (ultra-weak grid condition); thus, the assessment results can cover all possible situations in practice. As it can be seen, under a lower grid SCR, the critical mode moves to a hazardous area under the conventional control method. Moreover, it covers a larger area, meaning higher sensitivity to grid SCR variation.

For example, as shown in Figure 7a, the system equipped with the conventional control system becomes unstable under a SCR lower than 1.37, even for a low PLL bandwidth ( $f_{PLL} = 10$  Hz). In contrast, the proposed control method employs a higher PLL bandwidth ( $f_{PLL} = 50$  Hz) and provides excellent stability margins under a wide range of SCR variations, from 10 to 1. The maximum damping factor is lower than  $-30$  rad/s under different grid conditions.

It is worth mentioning that employing a high PLL bandwidth provided by the proposed control method is essential for good FRT capability and disturbance rejection.

(2) Figure 7b investigates the impact of different PLL bandwidths under the SCR = 1.5. The system under the conventional control method becomes unstable for PLL bandwidths higher than 17 Hz, while the proposed control method remains stable for all considered ones. Moreover, the critical mode covers a large area under the conventional ones, meaning higher sensitivity to the PLL bandwidths and severe control loops interaction. In contrast, the impact of the synchronization block on the system's critical mode is considerably reduced under the proposed control method.

It is worth noting that, unlike the grid SCR, the PLL bandwidth is a known and, usually, fixed parameter; thus, the design procedure can be performed for the desired value of PLL bandwidth to guarantee the required stability margin and the optimal control gain calculation, as shown in Figure 7a,c.

However, additional functionalities are recently suggested for VSCs to support power grids, e.g., transient stability enhancement, virtual inertia implementation, and fault ride-through capability. To obtain these objectives, the VSC may be equipped with a PLL designed with adaptive or gain scheduling techniques. In addition, it would be interesting to know how the PLL bandwidth can affect the system response under the proposed control method and the possibility of implementing a fast PLL. They can be considered reasons to provide Figure 7b.

(3) The operational point variations on the system stability should also be investigated since the linearized model around the specific operating point is used to calculate the control gains. As shown in Figure 7c, the inverter power level under a weak grid condition (SCR = 1.5) affects the damping factor and frequency of oscillations; however, the system remains stable under different power levels and both control methods. Under the conventional control method, increasing the inverter power level reduces the stability margin due to higher coupling and interaction between different control loops, VSC, and the power grid. Moreover, the frequency of oscillation is higher at lower powers and vice versa. It can be supposed that the control system's high-frequency parts contribute to the critical mode at lower loading. Moreover, low-frequency control parts affect the critical mode at higher loading. Finally, note that the stability margin is linearly improved under the proposed control method by increasing the inverter power level from lower values to nominal. The reason is that the optimal control gain is calculated for the nominal power, and calculated control gain can provide the optimal performance under this condition. Therefore, we can expect stability to deteriorate as the power level moves away from the nominal value.

### 3.3. Control Gain Matrix Simplification

The state-feedback-based active damping can considerably improve system performance and robustness, as presented in previous subsections. However, grid-side current sensors are required, and computations are increased due to employing all states.

Therefore, it would be worth investigating how the number of sensors and calculations can be reduced. A rational solution is employing a full- or reduced-order Luenberger observer and Kalman filter to eliminate the grid-side sensors. However, it increases the

computations and adds additional observer gains that should be tuned, leading to the higher complexity of the control system design and implementation. In this subsection, a more straightforward solution is proposed. First, it is assumed that all states are available, and the optimal control gain matrix is calculated.

Then it is assumed that the  $m$ th state is not available, so the related feedback gains are set to zero ( $x_m : \text{off} \rightarrow K_f(:, m) = 0$ ). Finally, the impact of eliminating this state on the system stability and performance is investigated by eigenvalues' analysis. If the critical mode and stability requirements have remained unchanged, this state can be simply excluded. Otherwise, this state and the related gains must be used. For example, if an eliminating grid-side current ( $i'_{gd}, i'_{gq}$ ) is required, the thirteenth and fourteenth columns of  $K_f$  must be set to zeros ( $x_{13} \& x_{14} : \text{off} \rightarrow K_f(:, 13 : 14) = 0$ ). Moreover, based on the new control gain matrix, the analysis of the eigenvalues can be carried out again.

Figure 8 shows the critical mode location when one of the states and its related gains are kept at zeros. The number next to each mode expresses the state number that is omitted. Moreover, 00 is equal to the case that all states are used. For example, as shown, eliminating states 8, 9, or 15 causes system instability, whereas when states 11, 13, or 14 are eliminated, the system remains stable. To examine the analytical results, time-domain simulations are presented in Figure 9.

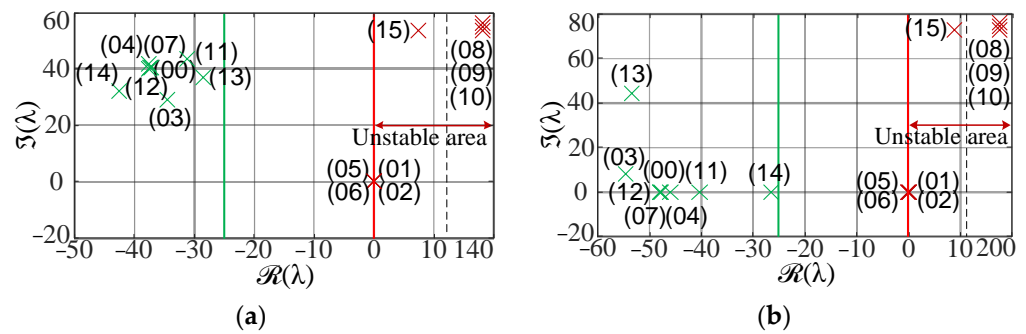


Figure 8. Critical mode locations of a grid-connected VSC in the complex s-plane (a) SCR = 1.5, and (b) SCR = 5.

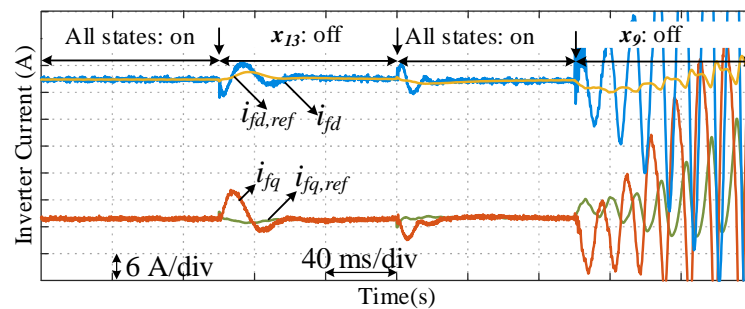


Figure 9. Time-domain simulations showing the system response under different control gain matrices.

This figure illustrates the system outputs under three different control gain matrices, where all states are available,  $x_{13}$  is not available ( $x_{13} : \text{off} \rightarrow K_f(:, 13) = 0$ ), and  $x_9$  is not available ( $x_9 : \text{off} \rightarrow K_f(:, 9) = 0$ ). As shown, eliminating  $x_{13}$  does not lead to system instability. On the other hand, eliminating  $x_9$  does.

As shown in Figure 8, there are seven states that eliminating them does not lead to system instability. It would be worth investigating the changes of critical mode locations where all of them are off simultaneously. This action reduces the number of employed states from 15 to 8.

Moreover, 46% of the control gain matrix elements become zeros, reducing computations:  $x_3, x_4, x_7, x_{11}, x_{12}, x_{13} \& x_{14} : \text{off} \rightarrow K_f(:, 3 : 4) = K_f(:, 7) = K_f(:, 11 : 14) = 0$ .

The impact of grid SCR variation on the critical mode under the conventional control method and the proposed full and reduced state-feedback control methods are examined in Figure 10. The system robustness is a little worse than full state feedback by reduced state feedback; as expected, however, it is still considerably better than the conventional one. In summary, the system remains stable under the reduced state feedback control, with a good stability margin over a wide range of grid SCR variations. At the same time, the possibility of implementing a high-performance PLL is achieved.

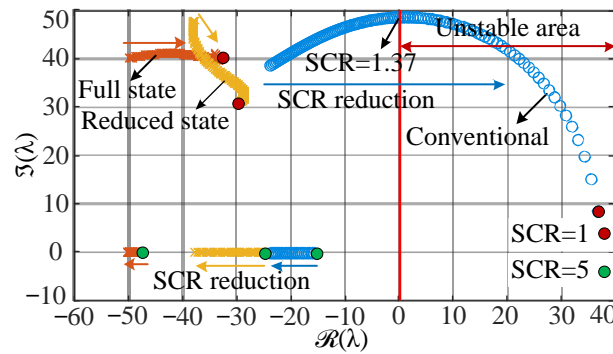


**Figure 10.** Impact of grid SCR variations on critical mode locations of a grid-connected VSC in the complex s-plane ( $P = P_n$  and  $f_{PLL} = 10$  Hz (conventional controller) and 50 Hz (proposed controllers)).

#### 4. Simulation and Experimental Results

In this section, we recount how simulation and experimental tests were carried out to validate the performance of the proposed control method and compare the results with the conventional one. The simulation model was prepared in MATLAB/Simulink with parameters as close as possible to the real power system. The control and system parameters are given in Table 3.

**Table 3.** Main system and control parameters.

Power System Parameters		Control Parameters	
Nominal power ( $P_n$ )	10 (kW)	Conventional control method	
Nominal line voltage ( $v_g$ )	400 (V)	$k_{pc}, k_{ic}$	$9.425, 4.4 \times 10^3$
Grid frequency ( $f_1$ )	50 (Hz)	$k_{pp}, k_{ip}$	0.22, 9.9
Filter capacitor ( $C_f$ )	10 ( $\mu$ F)	$k_{pa}, k_{ia}$	0, 4.8
Inverter-side inductor ( $L_f$ )	2 (mH)	$k_a, \omega_a$	$1, 6.6 \times 10^3$
Grid-side inductor ( $L_g$ )	5–50 (mH)	$k_{pd}, k_{id}$	0.13, 2.91
Grid SCR	1–10	$k_{ig}$	6.1
The series resistance of $C_f$ ( $r_c$ )	0.5 (m $\Omega$ )	Proposed control method	
The series resistance of $L_f$ ( $r_f$ )	1 (m $\Omega$ )	$1.5, 1 \times 10^4$	$r, q_1$
The series resistance of $L_g$ ( $r_g$ )	1 (m $\Omega$ )	1, 5	$q_2, q_3$
DC-link capacitor ( $C_{dc}$ )	1.5 [mF]	0.22, 9.9	$k_{pp}, k_{ip}$
DC-link voltage ( $v_{dc}$ )	700 (V)	Control delay	
Sampling and switching frequencies	10 (kHz)	150 ( $\mu$ s)	$T_d$

Based on that, various analyses and tests were carried out to reveal system performance under different conditions, which might not be possible by experiments due to some practical limitations (e.g., large inductors values, power, and current limitations). Finally, analytical and simulation results were validated by conducting experiments on a laboratory setup. It is worth noting that a downscaled power system is designed to emulate weak grid



conditions and reduce the required inductors in practice. Table 4 shows the parameters that differ from the main circuit parameters. The common parameters by the main circuit are not repeated in this table.

**Table 4.** Downscaled system and control parameters.

Power System Parameters		Control Parameters	
Nominal power ( $P_n$ )	5 (kW)	Conventional control method	
Nominal line voltage ( $v_g$ )	172 (V)	$k_{pc}, k_{ic}$	7.068, $3.3 \times 10^3$
Filter capacitor ( $C_f$ )	30 ( $\mu\text{F}$ )	$k_{pp}, k_{ip}$	0.51, 22.95
Inverter-side inductor ( $L_f$ )	1.5 (mH)	$k_{pa}, k_{ia}$	0, 30
Grid-side inductor ( $L_g$ )	1.9–19 (mH)	$k_{ig}$	3
DC-link voltage ( $v_{dc}$ )	600 (V)	Proposed control method	
$r, q_1$	$2, 1 \times 10^4$	$k_{pp}, k_{ip}$	0.51, 22.95
		$q_2, q_3$	1, 1

The experimental setup includes two 5 kW Danfoss voltage source converters operating back-to-back, LCL filters, a grid simulator (Chroma 61845), and a DS1007 dSPACE system, as shown in Figure 11.

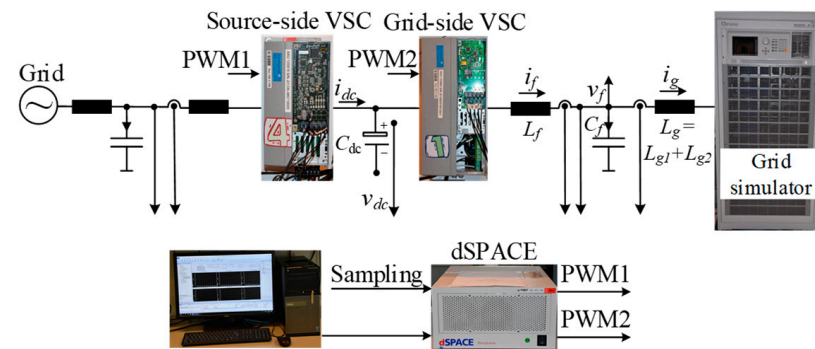


**Figure 11.** Experimental setup.

The first VSC acts as a constant power source, emulating a primary source such as PV or wind turbine and supplies the second three-phase grid-connected VSC.

The second VSC is connected to a grid simulator through an LCL filter and transfers the received power to the power grid. It contains CC, VFF, PLL, AVC, and DVC. A DS1007 dSPACE system platform is used to realize both control methods and drive VSCs.

Figure 12 shows the steady-state performance of the proposed control method under strong and ultra-weak grid conditions ( $\text{SCR} = 10$  and  $1$ ). This figure confirms a robust and stable operation over a wide range of grid SCR variations, especially critical scenario ( $\text{SCR} = 1$ ), while a high-performance PLL is implemented.

The system responses of the conventional and the proposed control methods under different grid SCRs are shown in Figure 13. As it can be seen, the performance of the conventional control method is degraded under a weaker grid, and it becomes unstable under the weakest one ( $\text{SCR} = 1.25$ ).

In comparison, the proposed control method can provide a stable response under weak grids. The simulation results also confirm the robustness analysis in the previous section.

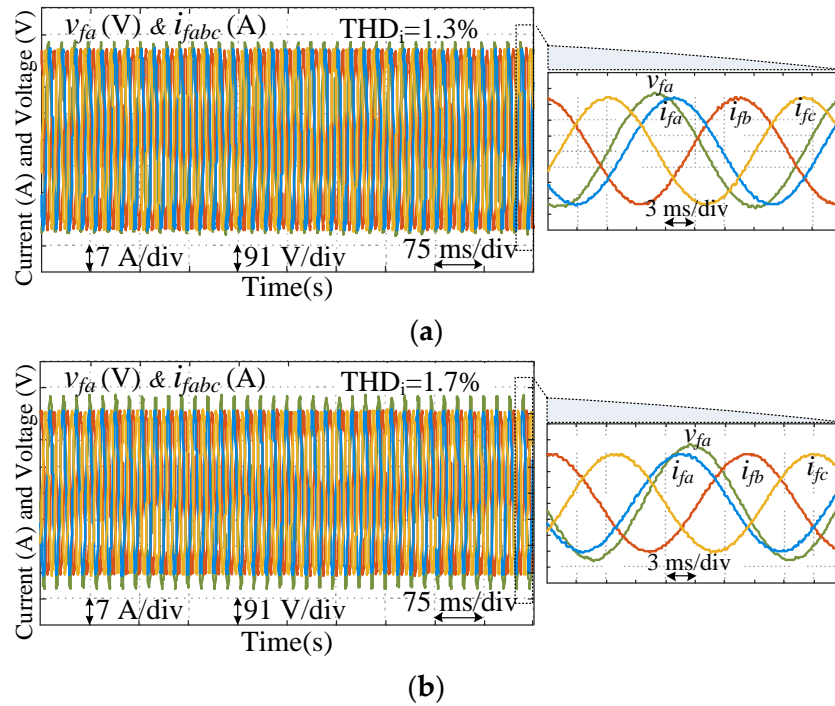


**Figure 12.** Time-domain simulations showing steady-state performance of the proposed state-feedback control method under different grid SCRs ( $P = 10 \text{ kW}$ ,  $f_{PLL} = 50\text{Hz}$ ): (a) SCR = 1 and (b) SCR = 10.

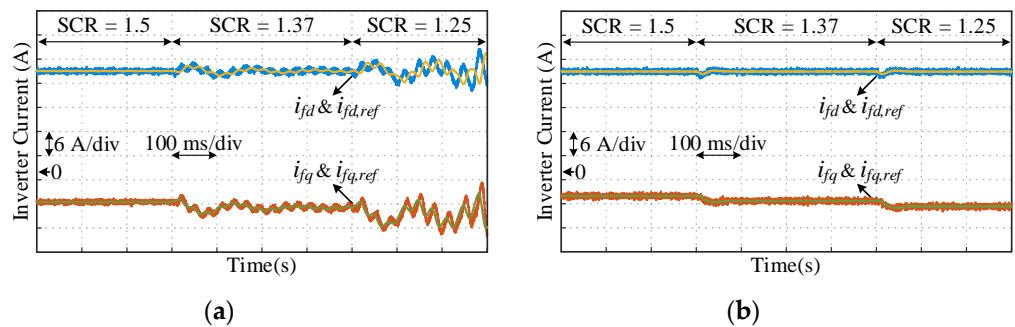


**Figure 13.** Time-domain simulations showing the system response under different grid SCR (SCR = 1.5, 1.35, and 1.25;  $P = 10 \text{ kW}$ ): (a) the conventional control method and (b) the proposed control method.

The system performance under different PLL bandwidths is investigated in Figure 14. As shown, under the conventional control method, it is impossible to implement fast PLL in weak grids. In contrast, the proposed control method can facilitate the implementation of high-performance and fast PLL. Moreover, the system is stable over a wide range of PLL bandwidth selections. Therefore, the PLL bandwidth can be selected based on the other performance requirements, such as fault ride-through (FRT) capability, large-signal stability, and ancillary services such as virtual inertia, and not only restricted limitations imposed by small-signal stability.

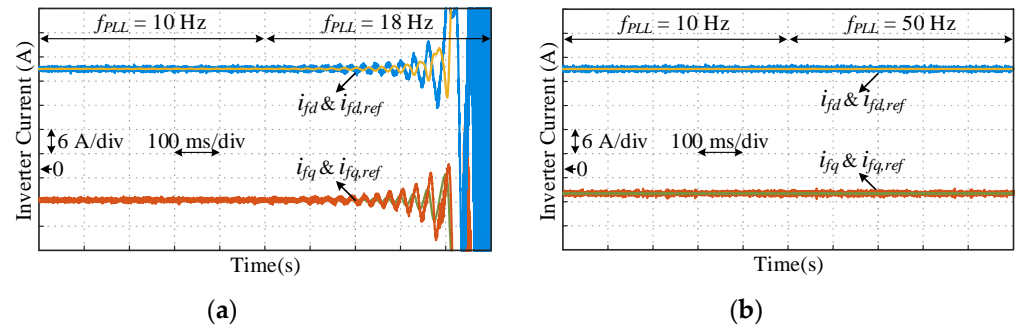


**Figure 14.** Time-domain simulations showing the system response under different PLL bandwidths ( $P = 10 \text{ kW}$ ,  $\text{SCR} = 1.5$ ): (a) the conventional control method and (b) the proposed control method.

The dynamic response of the VSC under 20% voltage sag at the grid voltage is depicted in Figure 15.

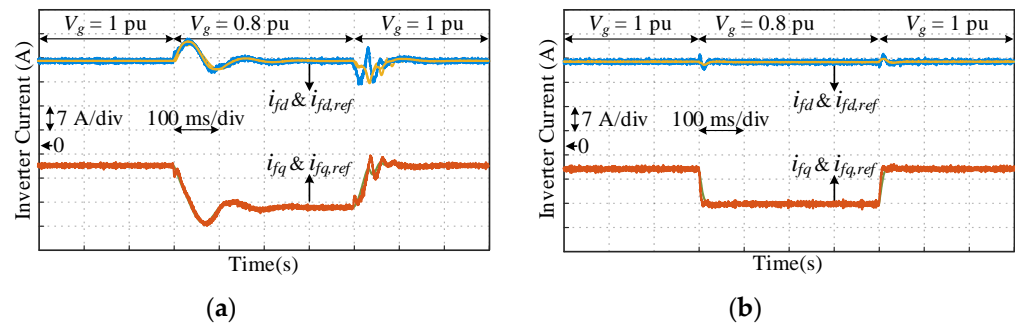


**Figure 15.** Time-domain simulations showing the system response under 20% voltage sag at the grid voltage ( $P = 10 \text{ kW}$ ,  $\text{SCR} = 2$ ): (a) the conventional control method and (b) the proposed control method.

The conventional control method has a larger rise time. However, it can be expected when outer voltage control loops are considered, and the system operates under a very weak grid connection, as discussed in References [23,32], where a rise time equal to or smaller than 100 ms was suggested for AVC as a compromise between the system stability and performance. In contrast, the proposed control method shows an excellent transient performance and disturbance-rejection capability that are even higher than the required levels by standards.

Furthermore, the transient performance of both control methods under step changes in the dc voltage reference is shown in Figure 16. Both control methods can provide a good transient response; however, the proposed one can respond a little faster with lower oscillations.

Finally, the feasibility of the proposed control method is examined in practice. The performance of both control methods under weak grid conditions ( $\text{SCR} = 1.21$ ) is shown in Figures 17 and 18. Experiments show their capability under different PLL bandwidths and 20% voltage sag. As shown, the proposed control method can employ a fast and high-performance PLL under weak grids, while the conventional one cannot. Moreover, the conventional one becomes unstable under a 20% voltage sag. In contrast, the proposed control method has an excellent disturbance rejection and fault ride-through capability.

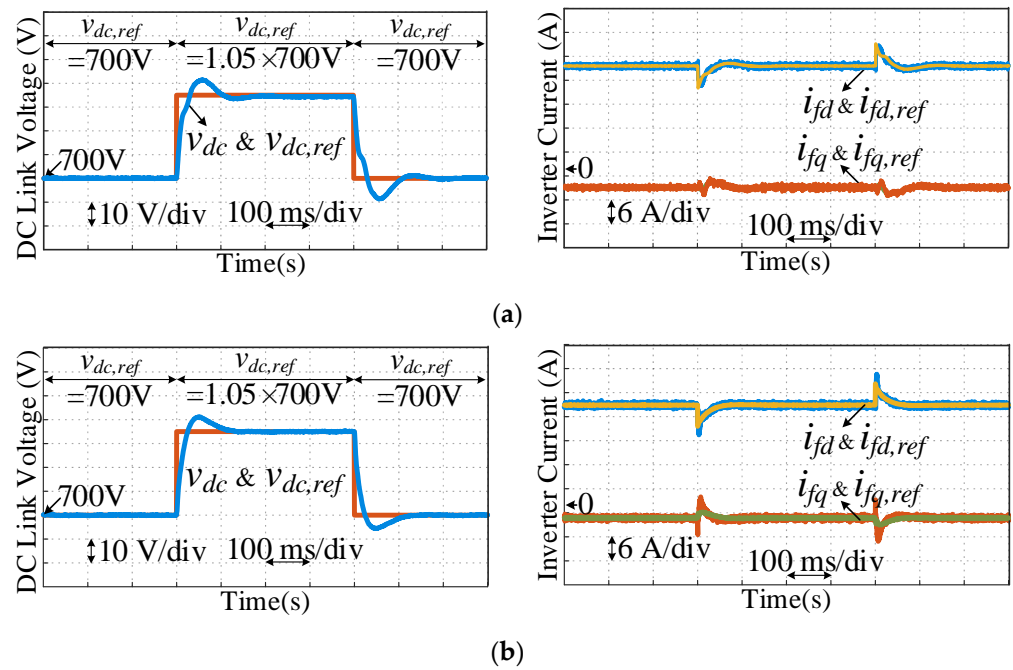


**Figure 16.** Time-domain simulations showing the system response under several step changes in the dc voltage reference ( $P = 10 \text{ kW}$ ,  $\text{SCR} = 2$ ): (a) the conventional control method and (b) the proposed control method.

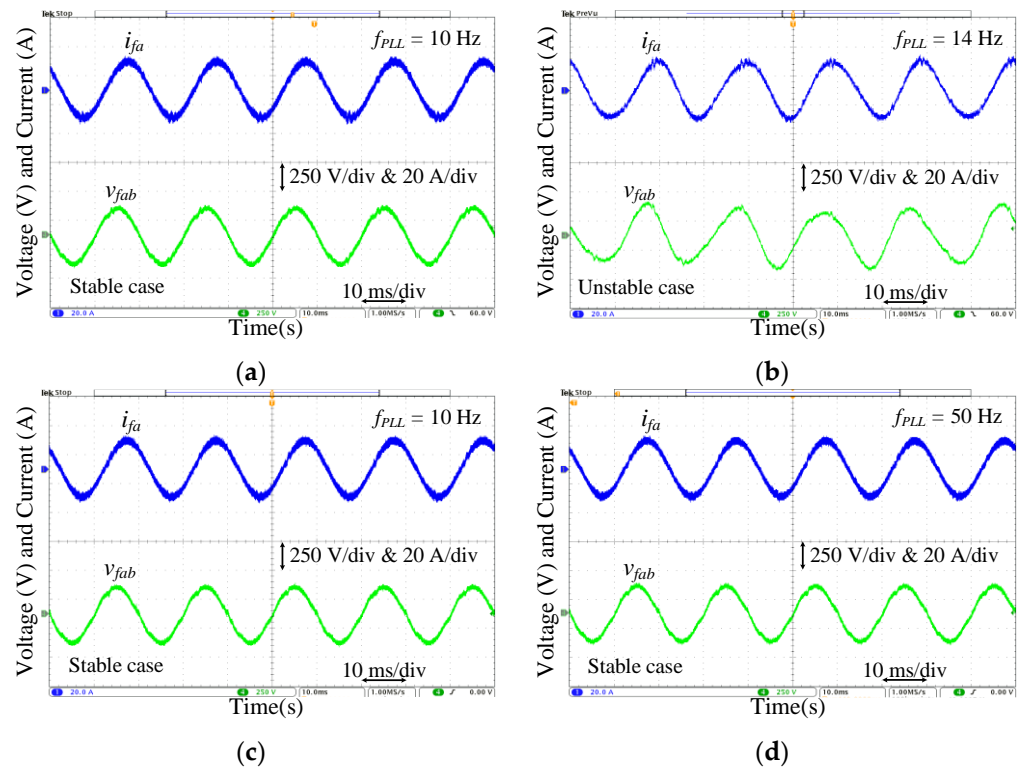


**Figure 17.** Experimental results showing the system response under different PLL bandwidths ( $\text{SCR} = 1.21$ ,  $L_g = 15.5 \text{ mH}$  and  $P = 5 \text{ kW}$ ): (a,b) the conventional control method and (c,d) the proposed control method.

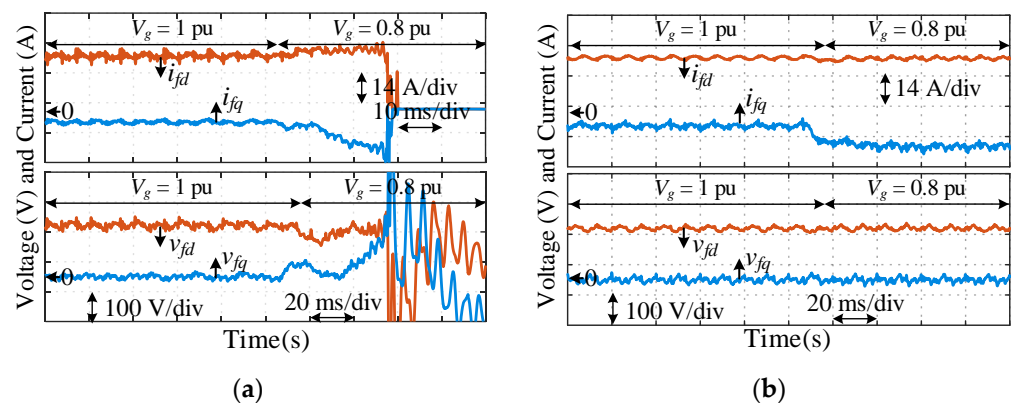


**Figure 18.** Experimental results showing the system response under 20% voltage sag at the grid voltage ( $SCR = 1.21$ ,  $L_g = 15.5$  mH, and  $P = 5$  kW): (a) the conventional control method ( $f_{PLL} = 10$  Hz) and (b) the proposed control method ( $f_{PLL} = 50$  Hz).

## 5. Conclusions

This paper proposes a new design approach for robust and optimal active damping control of voltage source converters (VSCs) for grid applications. Based on the proposed formulation, all control gains are considered in one control gain matrix, leading to a linear optimization problem. Then different state-of-the-art techniques can be employed to calculate control gains in such a way the control system meets the desired stability and performance criteria. Among others, this paper used the linear-quadratic regulator (LQR) to calculate all control gains optimally and straightforwardly. In this respect, almost direct relationships between the tuning parameters and stability and performance indices such as maximum damping factor, minimum damping ratio and control gain matrix are identified, which considerably reduces the iterative process in the conventional control system design.

Thanks to the proposed control structure and optimal control gains calculation, the proposed method provides a fast dynamic response and significantly increases the system robustness and disturbance rejection capability under ultra-weak grid conditions. For example, the possibility of implementing a PLL bandwidth of more than 50 Hz under a grid SCR lower than two is obtained, which effectively suppresses disturbances on the control system and conducts fault ride-through of grid-connected VSCs.

The performance of the proposed control method under different operating conditions is comprehensively investigated by simulations and experiments and compared with the conventional one. The obtained results demonstrate the performance of the proposed control method under various operating conditions.

For future works, an extension of the proposed methodology to other VSC-based power system applications, such as active power filters and uninterruptible power supplies, is recommended. For these applications, extra resonators at desired harmonics are required to compensate for nonlinear loads, making the control system design difficult.

**Author Contributions:** Conceptualization, H.G.-K., P.D., C.W. and F.B.; methodology, H.G.-K.; software, H.G.-K.; validation, H.G.-K.; formal analysis, H.G.-K. and P.D.; investigation, H.G.-K., P.D., C.W. and F.B.; resources, P.D. and F.B.; data curation, H.G.-K.; writing—original draft preparation, H.G.-K.; writing—review and editing, H.G.-K., P.D., C.W. and F.B.; visualization, H.G.-K.; supervision, F.B., P.D. and C.W.; project administration, H.G.-K.; funding acquisition, F.B. and P.D. All authors have read and agreed to the published version of the manuscript.

**Funding:** This work is supported by the Reliable Power Electronic-Based Power System project at AAU Energy, Aalborg University, Aalborg, Denmark, as a part of the Villum Investigator Program funded by the Villum Foundation.

**Institutional Review Board Statement:** Not applicable.

**Informed Consent Statement:** Not applicable.

**Data Availability Statement:** Not applicable.

**Conflicts of Interest:** The authors declare no conflict of interest.

## References

- Farrokhhabadi, M.; Lagos, D.; Wies, R.W.; Paolone, M.; Liserre, M.; Meegahapola, L.; Kabalan, M.; Hajimiragha, A.H.; Peralta, D.; Elizondo, M.A.; et al. Microgrid Stability Definitions, Analysis, and Examples. *IEEE Trans. Power Syst.* **2020**, *35*, 13–29. [\[CrossRef\]](#)
- Ma, R.; Qiu, Q.; Kurths, J.; Zhan, M. Fast-Slow-Scale Interaction Induced Parallel Resonance and Its Suppression in Voltage Source Converters. *IEEE Access* **2021**, *9*, 90126–90141. [\[CrossRef\]](#)
- Liao, Y.; Wang, X. Stationary-Frame Complex-Valued Frequency-Domain Modeling of Three-Phase Power Converters. *IEEE J. Emerg. Sel. Top. Power Electron.* **2020**, *8*, 1922–1933. [\[CrossRef\]](#)
- Gholami-Khesht, H.; Davari, P.; Blaabjerg, F. Adaptive Predictive-DPC for LCL-Filtered Grid Connected VSC with Reduced Number of Sensors. In Proceedings of the 2020 22nd European Conference on Power Electronics and Applications (EPE'20 ECCE Europe), Lyon, France, 7–11 September 2020; pp. 1–10. [\[CrossRef\]](#)
- Zhang, C.; Cai, X.; Rygg, A.; Molinas, M. Sequence Domain SISO Equivalent Models of a Grid-Tied Voltage Source Converter System for Small-Signal Stability Analysis. *IEEE Trans. Energy Convers.* **2018**, *33*, 741–749. [\[CrossRef\]](#)
- Gong, H.; Wang, X.; Yang, D. DQ-Frame Impedance Measurement of Three-Phase Converters Using Time-Domain MIMO Parametric Identification. *IEEE Trans. Power Electron.* **2021**, *36*, 2131–2142. [\[CrossRef\]](#)
- Hans, F.; Schumacher, W.; Chou, S.-F.; Wang, X. Design of Multifrequency Proportional–Resonant Current Controllers for Voltage-Source Converters. *IEEE Trans. Power Electron.* **2020**, *35*, 13573–13589. [\[CrossRef\]](#)
- Lu, M.; Al-Durra, A.; Mueen, S.M.; Leng, S.; Loh, P.C.; Blaabjerg, F. Benchmarking of Stability and Robustness against Grid Impedance Variation for LCL-Filtered Grid-Interfacing Inverters. *IEEE Trans. Power Electron.* **2018**, *33*, 9033–9046. [\[CrossRef\]](#)
- Wang, X.; Blaabjerg, F.; Loh, P.C. Grid-Current-Feedback Active Damping for LCL Resonance in Grid-Connected Voltage-Source Converters. *IEEE Trans. Power Electron.* **2016**, *31*, 213–223. [\[CrossRef\]](#)
- Wu, H.; Wang, X. Virtual-Flux-Based Passivation of Current Control for Grid-Connected VSCs. *IEEE Trans. Power Electron.* **2020**, *35*, 12673–12677. [\[CrossRef\]](#)
- Gong, H.; Wang, X.; Harnefors, L.; Hasler, J.-P.; Danielsson, C. Admittance-Dissipativity Analysis and Shaping of Dual-Sequence Current Control for VSCs. *IEEE J. Emerg. Sel. Top. Power Electron.* **2022**, *10*, 324–335. [\[CrossRef\]](#)
- Mahafugur Rahman, F.M.; Pirsto, V.; Kukkola, J.; Routimo, M.; Hinkkanen, M. State-Space Control for LCL Filters: Converter versus Grid Current Measurement. *IEEE Trans. Ind. Appl.* **2020**, *56*, 6608–6618. [\[CrossRef\]](#)
- Khajehoddin, S.A.; Karimi-Ghartemani, M.; Ebrahimi, M. Optimal and Systematic Design of Current Controller for Grid-Connected Inverters. *IEEE J. Emerg. Sel. Top. Power Electron.* **2018**, *6*, 812–824. [\[CrossRef\]](#)
- Ahmedi, A.; Mohammadi-Ivatloo, B.; Anvari-Moghaddam, A.; Marzband, M. Optimal Robust LQI Controller Design for Z-Source Inverters. *Appl. Sci.* **2020**, *10*, 7260. [\[CrossRef\]](#)
- Maccari, L.A.; Massing, J.R.; Schuch, L.; Rech, C.; Pinheiro, H.; Oliveira, R.C.L.F.; Montagner, V.F. LMI-Based Control for Grid-Connected Converters with LCL Filters under Uncertain Parameters. *IEEE Trans. Power Electron.* **2014**, *29*, 3776–3785. [\[CrossRef\]](#)
- Koch, G.G.; Osorio, C.R.D.; Pinheiro, H.; Oliveira, R.C.L.F.; Montagner, V.F. Design Procedure Combining Linear Matrix Inequalities and Genetic Algorithm for Robust Control of Grid-Connected Converters. *IEEE Trans. Ind. Appl.* **2020**, *56*, 1896–1906. [\[CrossRef\]](#)
- Koch, G.G.; Maccari, L.A.; Oliveira, R.C.L.F.; Montagner, V.F. Robust  $H_{\infty}$  State Feedback Controllers Based on Linear Matrix Inequalities Applied to Grid-Connected Converters. *IEEE Trans. Ind. Electron.* **2019**, *66*, 6021–6031. [\[CrossRef\]](#)
- Bimarta, R.; Kim, K.-H. A Robust Frequency-Adaptive Current Control of a Grid-Connected Inverter Based on LMI-LQR under Polytopic Uncertainties. *IEEE Access* **2020**, *8*, 28756–28773. [\[CrossRef\]](#)
- Gholami-Khesht, H.; Davari, P.; Novak, M.; Blaabjerg, F. Robust  $H_{\infty}$  Current Control of Three-Phase Grid-Connected Voltage Source Converters Using Linear Matrix Inequalities. In Proceedings of the 2021 IEEE 22nd Workshop on Control and Modelling of Power Electronics (COMPEL), Cartagena, Colombia, 2–5 November 2021; pp. 1–6.
- Cecati, F.; Zhu, R.; Liserre, M.; Wang, X. State-Feedback-Based Low-Frequency Active Damping for VSC Operating in Weak-Grid Conditions. In Proceedings of the 2020 IEEE Energy Conversion Congress and Exposition (ECCE), Detroit, MI, USA, 11–15 October 2020; pp. 4762–4767. [\[CrossRef\]](#)
- Zhou, S.; Zou, X.; Zhu, D.; Tong, L.; Zhao, Y.; Kang, Y.; Yuan, X. An Improved Design of Current Controller for LCL-Type Grid-Connected Converter to Reduce Negative Effect of PLL in Weak Grid. *IEEE J. Emerg. Sel. Top. Power Electron.* **2018**, *6*, 648–663. [\[CrossRef\]](#)
- Silwal, S.; Taghizadeh, S.; Karimi-Ghartemani, M.; Hossain, M.J.; Davari, M. An Enhanced Control System for Single-Phase Inverters Interfaced with Weak and Distorted Grids. *IEEE Trans. Power Electron.* **2019**, *34*, 12538–12551. [\[CrossRef\]](#)
- Zhang, H.; Harnefors, L.; Wang, X.; Hasler, J.-P.; Ostlund, S.; Danielsson, C.; Gong, H. Loop-at-a-Time Stability Analysis for Grid-Connected Voltage-Source Converters. *IEEE J. Emerg. Sel. Top. Power Electron.* **2021**, *9*, 5807–5821. [\[CrossRef\]](#)
- Huang, L.; Xin, H.; Dorfler, F.  $H_{\infty}$ -Control of Grid-Connected Converters: Design, Objectives and Decentralized Stability Certificates. *IEEE Trans. Smart Grid* **2020**, *11*, 3805–3816. [\[CrossRef\]](#)

25. Yang, D.; Wang, X. Unified Modular State-Space Modeling of Grid-Connected Voltage-Source Converters. *IEEE Trans. Power Electron.* **2020**, *35*, 9700–9715. [[CrossRef](#)]
26. De Bosio, F.; De Souza Ribeiro, L.A.; Freijedo, F.D.; Pastorelli, M.; Guerrero, J.M. Effect of State Feedback Coupling and System Delays on the Transient Performance of Stand-Alone VSI with LC Output Filter. *IEEE Trans. Ind. Electron.* **2016**, *63*, 4909–4918. [[CrossRef](#)]
27. Pogaku, N.; Prodanovic, M.; Green, T.C. Modeling, Analysis and Testing of Autonomous Operation of an Inverter-Based Microgrid. *IEEE Trans. Power Electron.* **2007**, *22*, 613–625. [[CrossRef](#)]
28. Hoffmann, N.; Fuchs, F.W. Minimal Invasive Equivalent Grid Impedance Estimation in Inductive–Resistive Power Networks Using Extended Kalman Filter. *IEEE Trans. Power Electron.* **2014**, *29*, 631–641. [[CrossRef](#)]
29. De Almeida, P.M.; Ribeiro, A.S.B.; Souza, I.D.N.; Fernandes, M.d.C.; Fogli, G.A.; Cuk, V.; Barbosa, P.G.; Ribeiro, P.F. Systematic Design of a DLQR Applied to Grid-Forming Converters. *IEEE J. Emerg. Sel. Top. Ind. Electron.* **2020**, *1*, 200–210. [[CrossRef](#)]
30. Yassami, H.; Darabi, A.; Rafiei, S.M.R. Power System Stabilizer Design Using Strength Pareto Multi-Objective Optimization Approach. *Electr. Power Syst. Res.* **2010**, *80*, 838–846. [[CrossRef](#)]
31. Khodabakhshian, A.; Hemmati, R. Multi-Machine Power System Stabilizer Design by Using Cultural Algorithms. *Int. J. Electr. Power Energy Syst.* **2013**, *44*, 571–580. [[CrossRef](#)]
32. *IEEE Std 1052-2018*; IEEE Guide for Specification of Transmission Static Synchronous Compensator (STATCOM) Systems. IEEE: Piscataway, NJ, USA, 2019; pp. 1–115.